

## **Validation of a coupled wave-flow model in a high-energy setting: the Mouth of the Columbia River.**

Edwin Elias<sup>1,2\*</sup>, Guy Gelfenbaum<sup>2</sup>, and Andre van der Westhuysen<sup>3</sup>

1. Deltares, P.O. Box 177, 2600 MH Delft, The Netherlands. [Edwin.elias@deltares.nl](mailto:Edwin.elias@deltares.nl). Corresponding author.

2. United States Geological Survey, Pacific Coastal and Marine Science Center, 400 Natural Bridges Drive, Santa Cruz, CA 95060, USA. [ggelfenbaum@usgs.gov](mailto:ggelfenbaum@usgs.gov)

3. Deltares, P.O. Box 177, 2600 MH Delft, The Netherlands. Now UCAR Visiting Scientist at NOAA/NWS/NCEP  
5200 Auth Road, Camp Springs, MD 20746-4303 [andre.vanderwesthuysen@noaa.gov](mailto:andre.vanderwesthuysen@noaa.gov)

**Keywords:** Process-based modeling, Columbia River, tidal inlet, Delft3D, wave-current interaction

## **Abstract**

A month-long time series of wave, current, salinity, and suspended-sediment measurements were made at five sites on a transect across the Mouth of Columbia River (MCR). These data were used to calibrate and evaluate the performance of a coupled hydrodynamic and wave model for the MCR based on the Delft3D modeling system. The MCR is a dynamic estuary inlet in which tidal currents, river discharge, and wave-driven currents are all important. Model tuning consisted primarily of spatial adjustments to bottom drag coefficients. In combination with (near-) default parameter settings, the MCR model application is able to simulate the dominant features in the tidal flow, salinity and wave fields observed in field measurements. The wave-orbital averaged method for representing the current velocity profile in the wave model is considered the most realistic for the MCR. The hydrodynamic model is particularly effective in reproducing the observed vertical residual and temporal variations in current structure. Density gradients introduce the observed and modeled reversal of the mean flow at the bed and augment mean and peak flow in the upper half of the water column. This implies that sediment transport during calmer summer conditions is controlled by density stratification and is likely net landward due to the reversal of flow near the bed. The correspondence between observed and modeled hydrodynamics make this application a tool to investigate hydrodynamics and associated sediment transport.

## 1. Introduction

Coastal management, planning and maintenance increasingly rely on numerical model predictions of hydrodynamics, sediment transport and morphodynamic change. Although of considerable disagreement among researchers in this field, recent studies by e.g. *Hibma* [2004], *van Maren* [2004], *Elias et al.* [2006], and *Lesser* [2009] suggest that process-based models can be successfully applied to model hydrodynamics and morphodynamics in complex tidal inlet systems. However, as tidal inlets with their rapid rates of water flow, sediment transport, and morphological change are challenging places to make observations, there is an absence of suitable field data sets that comprise sufficient and coherent observations for model validation. The United States Army Corps of Engineers (USACE) in collaboration with the United States Geological Survey (USGS) conducted the “Mega Transect Experiment” (MGT) during the summer of 2005 in the Mouth of the Columbia River (MCR). One of the specific goals of the MGT measurements was to provide observations suitable to evaluate the model skill of a process-based model. In combination with hydrographic observations at gaging stations in the estuary and upriver, and waves at an offshore buoy, the combined set of flow, waves, salinity and sediment transport measurements in such complex and energetic inlet mouth provide an excellent model validation case.

The Columbia River, draining a 669,000 square kilometers watershed, is the largest river on the Pacific coast of the United States (see Figure 1 for location). Aligned by entrance jetties, the MCR and its continuously dredged entrance channel provides safe passage for shipping, forms a vital connection for salmon migration [*Casillas*, 1999], and links the sediment exchange from the river basin to the Columbia River littoral cell [*Kaminsky et al.*, 2010]. One of the characteristic features of the MCR is the buoyant

plume created by the large Columbia River outflow into the Pacific. The dynamics of the Columbia River plume have been studied extensively [*Barnes et al.*, 1972; *Jay and Smith*, 1990; *Hickey*, 1998; *Hickey et al.*, 2005; *Orton and Jay*, 2005; *Horner-Devine*, 2008; *Horner-Devine et al.*, 2009]. Recently, coastal margin observatories CORIE [*Baptista*, 2006], now SATURN/CORIE, large research programs (RISE, CREDDP), and several numerical applications were completed. *Hickey et al.* [2010] summarize recent findings from the RISE (River Influences on Shelf Ecosystems) project, while major advances understanding of the hydrology, sedimentology, and ecology of the estuary were made earlier through the CREDDP - Columbia River Estuary Data Development Program (*Hamilton*, 1990; *Jay and Smith*, 1990; *Jay et al.*, 1990; *Sherwood and Creager*, 1990; *Sherwood et al.*, 1990). Numerical modeling started with salinity and circulation modeling by *Hamilton* [1990] using a laterally averaged estuary model, and has advanced to three-dimensional circulation models without the influence of waves [*Baptista et al.*, 2005; *Zhang and Baptista*, 2008; *Banas et al.*, 2009; *Liu et al.*, 2009a,b; *MacCready et al.*, 2009; *Burla et al.*, 2010]. No attempt has yet been made to model the transport of sand in the MCR, which requires successfully modeling the waves and the three dimensional currents.. Improved understanding of the sediment exchange (mechanisms) between estuary and ocean is seen as crucial to understand the observed (locally severe) erosion of the adjacent coasts and Jetty foundation [*Gelfenbaum and Kaminsky*, 2010].

In principle, the process-based numerical model Delft3D [*Stelling*, 1984; *Lesser et al.*, 2004) contains the necessary physical processes and formulations to compute hydrodynamics and sediment transport under influence of a buoyant plume interacting with strong tidal currents and a severe wave climate. Extensive validation of the Delft3D

flow and sediment transport equations has been performed with laboratory data and case studies [summarized in *Lesser et al.*, 2004 and *Gerritsen et al.*, 2007]. World-wide case studies indicate that Delft3D is accurate in a wide range of applications. Comparison of model results with dedicated field campaigns such as Coast3D [*Elias et al.*, 2000; *Walstra et al.*, 2000; *Klein et al.*, 2001; *Sutherland et al.*, 2004) and DUCK [*Morris*, 2001; *Hsu et al.*, 2008] indicate that near-shore hydrodynamics and sediment dynamics can be computed accurately. Waves and wave-flow coupling have been tested by *Walstra et al.* [2000] and compared to field measurements by *Mulligan et al.* [2008; 2010]. Plume dynamics were investigated by *Mulligan et al.* (2011). A dedicated calibration and validation study of the Delft3d model on the combined forcing of waves, tides and estuarine circulation at a high-energetic estuary mouth is to our knowledge not yet documented.

In the current study, presented in two parts, the MGT data set was used to validate and calibrate a coupled Delft3D-SWAN hydrodynamic, wave and sediment transport model setup for sand-sized sediment. Although the Delft3D model system is used, the presented field data provides a unique validation dataset for similar type systems. The study area and MGT field data are briefly described in Section 2. The numerical model formulations and MCR application are discussed in Section 3. Section 4 presents the results of calibration of the hydrodynamic and wave models. The focus in the wave model calibration is on the realistic representation of the three-dimensional current field in SWAN as *Groeneweg et al.* [2008] and *Van Vledder et al.* [2008], amongst others, have shown the significant influence of currents on wave prediction by SWAN [*Booij et al.*,

1999] in tidal inlets. The conclusion (Section 5) of this study is that based on a calibration of the bed roughness in combination with default settings, the flow model yielded good agreement in surface elevation, flow and salinity at the MCR and through the estuary. The agreement between observed and modeled hydrodynamics makes this application a tool to investigate hydrodynamics and associated sediment transport in future applications (part 2 of this study described in a subsequent paper).

## **2. Study Site and Field Data**

### *2.1. Study Location*

The MCR provides access between the Pacific Ocean and the Columbia River making this an important connection for commercial and recreational activities (Figure 2). The MCR is also vital for the reproduction cycle of Columbia River salmon that travel from the Columbia River to the Pacific as juveniles and back to their spawning grounds as adults. Over thousands of years the river has supplied much of the sand that forms the beaches and estuaries of the Columbia River littoral cell, formed by the southwest Washington and northwest Oregon coast [Gelfenbaum and Kaminsky, 2010]. Since the early 20<sup>th</sup> century the river hydrodynamics and morphodynamics have been significantly altered to facilitate navigation (e.g. construction of entrance jetties and dredging in the entrance and estuary), while over 200 dams built for irrigation, power generation, and flood control changed the rivers hydrograph and sediment load [Sherwood *et al.*, 1990; Gelfenbaum *et al.*, 1999; Mikhailova, 2008]. Gelfenbaum *et al.* [1999] calculate that as a result of flow regulation and flood control the fluvial sand supply to the estuary decreased

from 4.3 million m<sup>3</sup>/year in the interval 1878– 1935 to 2.6 million m<sup>3</sup>/year during 1935–1958, and down to 1.4 million m<sup>3</sup>/year in 1958–1997.

Prior to jetty construction, the tidal channels through the MCR shifted north and south between Fort Stevens and Cape Disappointment (Figure 2), and varied in depth between 18 to 25 feet deep below MLLW. Ships faced a difficult task traversing the Columbia River bar (ebb-tidal delta) due to severe and unpredictable wave conditions and shifting tidal channels and shoals. The construction of entrance jetties, South Jetty between 1885 and 1895, North Jetty between 1913 and 1917, and Jetty A in 1939, improved navigation through the MCR, but also significantly altered the inlet morphology. The ebb-tidal delta moved offshore into deeper water by about 3 km [*Kaminsky et al.*, 2010]. In addition, the main channel deepened and stabilized in position, although annual maintenance dredging is still required to keep the channel at its required depth of nearly 17 m (55 ft.). Based on the analysis of bathymetric maps, *Moritz et al.* [2003] conclude that between 1885 and 1925 375 to 600 million m<sup>3</sup> of sand was pushed out of the MCR and estuary. Rapid initial accretion along the beaches near the Columbia River mouth was followed by equally rapid shoreline retreat since the early 1950s [*Hickson*, 1936; *Buisman et al.*, 2003; *Moritz et al.*, 2003; *Gelfenbaum and Kaminsky*, 2010; *Kaminsky et al.*, 2010].

The severe wave and tide climate impacting the MCR made frequent repairs of the North and South Jetties necessary [*Ward*, 1988; *Byrnes et al.*, 2007]; the latest repairs occurred in 2005 on the North Jetty and 2006-2007 on the South Jetty. Despite intermittent repair and partial rehabilitation efforts, all of the MCR jetties are currently in deteriorated condition (Batelle, 2011). One of the issues is scour of the Jetty foundation,

and severe hot-spot erosion at the adjacent shorelines of Cape Disappointment (Benson Beach) and Clatsop Spit.

The reversal from overall accretion along the adjacent coast in the past to varying degrees of localized erosion at present is not fully understood. Strategically placing dredged materials at the Mouth of the Columbia River (MCR) could help reduce local sand deficits and shoreline retreat, but basic understanding of the sediment transport pathways needs to be improved to select the appropriate disposal locations and to adopt a sustainable maintenance strategy. The sediment transport model presented in this paper can help examine and isolate the physical processes responsible for sediment transport and morphological change in this dynamic estuary entrance.

### *2.1. Forcing Conditions*

A severe wind and wave climate, a large tidal range and tidal currents, substantial river discharge and plume dynamics affect nearshore hydrodynamics and sediment transports at MCR [*Hickey and Banas, 2003; Hickey et al., 2005 ; Styles, 2006; Spahn, 2009*]. River flows are highly regulated at upstream dams, resulting in an annual mean flow of 7300 at The Dalles, with seasonal variations ranging from  $2.5 - 11 \times 10^3 \text{ m}^3/\text{s}$  [*Bottom et al., 2005*].

Ocean tides are mixed semi-diurnal with a mean tidal range of 2.4 m, and a 28-day lunar variation of spring and neap tides in the 2 to 4 m range (Figure 3a). Peak tidal velocities in the narrow entrance channel typically attain 2.6 m/s, but often exceed 3 m/s during peak ebb tides and high river discharge. In the estuary the fresh river flow and salty ocean tides converge, creating a turbulent water circulation [*Jay and Smith, 1990*] and a buoyant outflow into the Pacific, the Columbia River plume [*Morgan et al., 2005*;

*Orton and Jay, 2005; Horner-Devine, 2008; Horner-Devine et al., 2009*]. The important plume source zone were low-saline waters lose contact with the seabed, roughly lies between the MCR jetties, although the location varies with tides, tidal range and river discharge. The far-field zone were final mixing with ambient seawater occurs may extend up to the Strait of Juan de Fuca in the north, and the Oregon-California border in the south depending on coastal circulation and weather conditions [*Hickey et al., 1998; Hickey and Banas, 2003; Horner-Devine et al., 2009*].

The interaction of the strong Columbia River outflow into the predominantly opposing westerly winds and ocean swells creates unpredictable conditions with large waves, making the MCR notoriously dangerous for boating and shipping. Waves are highest during winter with an average significant wave height around 3 m and periods of 12 s from the southwest. However, storms wave heights can reach up to 14 m just outside the ebb-delta. During summer (May-August) waves are smaller with an average of 1.2 m at 8 s and predominantly from the west-northwest [*Ruggiero et al., 1997; Tillotson and Komar, 1997; Allan and Komar, 2000*]. Such conditions were observed during the MGT experiment (Figure 3 and Figure 4).

### 2.3 *The USACE Mega Transect experiment*

The USACE Mega-Transect experiment (MGT) provides a comprehensive dataset for hydrodynamic, wave and sediment model validation [*Moritz et al., 2007*]. The MGT was designed to quantify the flux of sand through the mouth of the estuary, and to elucidate important processes acting in the estuary entrance by deploying an array of five tripods across the entrance (labeled MGT 1 – 5 in Figure 2). Tripods were 2-3 m tall and

equipped with upward-looking ADPs and ADCPs to measure velocity profiles and waves, ADVs to measure near-bottom currents and near-bed wave motions (Figure 5). Salinity and sediment transport concentrations were obtained using CTD and OBS instruments. Data were collected from 3 August – 9 September 2005, with the exception of MGT 3, in which the time series were truncated as the tripod was dragged offsite and toppled over by the tow-line of a passing barge and container ship on August 16th.

The upward looking Sontek ADPs at stations 1 and 2 sampled velocity half hourly at a 1 Hz frequency and 5 minute burst length at 1500 kHz and 500 kHz respectively. ADCPs at stations 4 and 5 were configured to measure velocities in 0.5 m bins. Five minute ensembles were taken at a 1 Hz frequency and 30 minute intervals. Instrument placement was approximately 2.4 m above the bed with a blanking distance of 0.88 m above the instrument. Using the heading, tilt and roll measurements of the internal compass, velocity measurements were rotated and stored in geographic coordinates of velocity (east, north, up). Waves were measured half hourly with 17 min bursts at 2 Hz. Time series of water levels for each station were obtained from the pressure sensors assuming a constant density over the water column. Acoustic Doppler Velocimeters (ADV) were placed closer to the bed, at 1.2 m, to measure near-bottom currents and orbital velocities. Conductivity, salinity and temperature were measured with a Microcat SBE (CTD). Estimates of the suspended sediment concentrations were obtained using two Optical Backscatter Sensors (OBS) on tripods 1, 2, 3 and 5. Each OBS was calibrated with sediment samples collected at the station to convert the counts into sediment concentrations in  $\text{kg/m}^3$  values.

Figure 4 presents time series of representative measurements taken at MGT 4 and 5 (more data are presented in the model validation section). The conditions encountered during the experiment were typical for summer conditions: a relatively small fresh-water inflow from the river (averaging  $4000 \text{ m}^3/\text{s}$ ), mild winds ( $0.2 - 9.2 \text{ m/s}$ ) and low to medium wind waves ( $0.64 - 2.41 \text{ m}$ ) predominantly from the Northwest (Figure 3e). The most salient features in the observations are: (1) the large tide range and significant (up to  $2.5 \text{ m/s}$ ) tidal velocities (Figure 4a, d), (2) the pronounced spring-neap variations in velocity magnitude, salinity and sediment transport rates (Figure 4c, d, f), and (3) the distinct modulations of the wave signal that correlate strongly with wave-current interaction as waves near double in height during strong opposing ebb currents (compare Figure 3d and Figure 4b). The time-series of suspended sediment concentrations and salinity correlate strongly to the spring-neap cycle. The largest sediment concentrations are observed during spring tides when velocities maximize (Figure 4f). The largest sediment transports are observed in the main channel (stations 2 and 3) due to larger velocities. The low wave energy observed during the experiment in combination with wave sheltering by the entrance jetties did not produce significant wave breaking and associated currents and transports on the shoals (stations 4 and 5). In general, the two OBS devices per tripod show a similar spring-neap fluctuation in sediment concentration, the differences at exact time points are a possible indication of the accuracy of the method and variability in the sediment flux rates. The salinity time series (Figure 4c) illustrate the large salinity variations that develop at the MCR. During neap to mean tides the MCR is relative salty with salinities ranging between 28 and 33 ppt. during ebb and flood respectively. During spring ebb-tide, the water column becomes more stratified

with salinity values dropping below 25 ppt. These observations are consistent with other observations in the Columbia River estuary [e.g. *Jay and Smith, 1990*]. Water temperatures (not shown) have a  $10^{\circ} C$  mean value but show significant daily and semi-diurnal variations in the  $7.5\text{--}15.5^{\circ} C$  range. During flood tide relatively cold ocean water (down to  $7.5^{\circ} C$ ) enters the MCR. In the shallow estuary, water temperature increases due to mixing and solar radiation resulting in temperatures up to  $15.5^{\circ} C$  during spring ebb conditions.

In addition to the MGT observations, long-term (continuous) measurements of waves and wind are made at an NDBC buoy (46029) located about 37 km west of the Columbia River entrance. Continuous discharge and water level are recorded upstream by the U.S. Geological Survey at Beaver Army Terminal near Quincy, OR. These additional wave and discharge observations are used as model boundary conditions. Salinity and water level measurements (CORIE\SATURN and NOAA) at various locations throughout the estuary are also used for model calibration. Figure 2 and Table 1 provide a complete overview of the locations and calibration data used.

### **3. Model Formulations and Model Setup**

The interaction of a substantial river discharge and prominent buoyant plume, large tidal range and strong tidal currents and a severe wind and wave climate make hydrodynamic and sediment modeling at MCR a challenging numerical modeling task. In principle, the process-based numerical model Delft3D [*Stelling, 1984; Lesser et al., 2004*] contains the necessary physical processes and formulations to account for: (a) complex stratification variations over the tidal and spring-neap cycle resulting from variations in the buoyancy flux of riverine inflow, advection by tides and the circulation

and mixing in the estuary; (b) wetting and drying of large tidal flats and other wetlands in the lower estuary; (c) wave-current interaction at the entrance [de Booi, 1999]; (d) sediment transports using the sediment transport models of *Van Rijn* [1993]. The main expressions of Delft3D-FLOW and SWAN are summarized below.

### 3.1. Hydrodynamic model

Delft3D-FLOW [Lesser *et al.*, 2004; Deltares, 2010b] solves the non-linear shallow-water equations derived from the three dimensional Navier Stokes equations for incompressible free surface flow (in 2D or 3D). For brevity we present the 2D basics here. By default, vertical accelerations are neglected reducing the vertical momentum equation to the hydrostatic pressure equation (eq. 1). The set of equations consists of (eq. 2, 3) the horizontal equations of motion wherein the horizontal pressure terms are given by Boussinesq approximations and the horizontal Reynold's stresses are based on the eddy viscosity concept, (eq. 4) the continuity equation, and (eq.5) the transport equations (here the  $k-\varepsilon$  turbulence closure model is used).  $M_x$  and  $M_y$  represent external sources or sinks of momentum (in these simulations the wave and wind stresses). See Lesser *et al.* (2004), Deltares (2010).

$$\frac{\partial P}{\partial \sigma} = -g\rho H \quad (1)$$

$$\begin{aligned} \frac{\partial U}{\partial t} + U \frac{\partial U}{\partial x} + V \frac{\partial U}{\partial y} + \frac{\omega}{h} \frac{\partial U}{\partial \sigma} - fV = \\ - \left( g \frac{\partial \zeta}{\partial x} + g \frac{h}{\rho_0} \int_{\sigma}^0 \left( \frac{\partial \rho}{\partial x} + \frac{\partial \sigma'}{\partial x} \frac{\partial \rho}{\partial \sigma'} \right) \partial \sigma' \right) + \nu_H \left( \frac{\partial^2 U}{\partial x^2} + \frac{\partial^2 U}{\partial y^2} \right) + M_x + \frac{1}{h^2} \frac{\partial}{\partial \sigma} \left( \nu_V \frac{\partial U}{\partial \sigma} \right) \end{aligned} \quad (2)$$

$$\begin{aligned} \frac{\partial V}{\partial t} + U \frac{\partial V}{\partial x} + V \frac{\partial V}{\partial y} + \frac{\omega}{h} \frac{\partial U}{\partial \sigma} - fU = \\ - \left( g \frac{\partial \zeta}{\partial y} + g \frac{h}{\rho_0} \int_{\sigma}^0 \left( \frac{\partial \rho}{\partial y} + \frac{\partial \sigma'}{\partial y} \frac{\partial \rho}{\partial \sigma'} \right) \partial \sigma' \right) + v_H \left( \frac{\partial^2 V}{\partial x^2} + \frac{\partial^2 V}{\partial y^2} \right) + M_y + \frac{1}{h^2} \frac{\partial}{\partial \sigma} \left( v_V \frac{\partial V}{\partial \sigma} \right) \end{aligned} \quad (3)$$

$$\frac{\partial \xi}{\partial t} + \frac{\partial [h\bar{U}]}{\partial x} + \frac{\partial [h\bar{V}]}{\partial y} = S \quad (4)$$

$$\begin{aligned} \frac{\partial [hc]}{\partial t} + \frac{\partial [hUc]}{\partial x} + \frac{\partial [hVc]}{\partial y} + \frac{\partial [\omega c]}{\partial \sigma} = \\ h \left[ \frac{\partial}{\partial x} \left( D_H \frac{\partial c}{\partial x} \right) + \frac{\partial}{\partial y} \left( D_H \frac{\partial c}{\partial y} \right) \right] + \frac{1}{h} \frac{\partial}{\partial \sigma} \left[ D_V \frac{\partial c}{\partial \sigma} \right] + hS \end{aligned} \quad (5)$$

In which:

$c$  mass concentration (kg/m<sup>3</sup>) of constituent (e.g salinity, sediment) modeled

$D_H, D_V$  horizontal and vertical diffusion coefficient (m<sup>2</sup>/s)

$f$  Coriolis coefficient (s<sup>-1</sup>)

$g$  gravitational acceleration (m/s<sup>2</sup>)

$h$  water depth (m)

$H$  total water depth (m)

$u, v, w$  horizontal and vertical Eulerian velocity components (m/s) in Cartesian coordinates

$U, V$  Generalized Lagrangian Mean (GLM) velocity components (m/s) for simulations including waves ( $U = u + u_s$  and  $V = v + v_s$  with  $u_s$  and  $v_s$  being the stokes drift components (Lesser et al., 2004)

$\bar{U}, \bar{V}$  depth-averaged GLM velocity components (m/s)

$S$  source and sink terms per unit area

$\nu_H, \nu_V$	horizontal and vertical kinematic viscosity ( $\text{m}^2/\text{s}$ )  for the $k$ - $\varepsilon$ model the eddy viscosity is modeled as $\nu_V = c'_\mu L \sqrt{k}$ with $c'_\mu$ and $c_D$ calibration constants, $k$ the turbulent kinetic energy, and the mixing length and $L = c_D \frac{k \sqrt{k}}{\varepsilon}$
$\rho$	fluid density ( $\text{kg}/\text{m}^3$ )
$\rho_0$	reference density of water ( $\text{kg}/\text{m}^3$ )
$\sigma$	vertical coordinate (m). In a Cartesian coordinate system: $(z - \xi) / H$
$\zeta$	water surface elevation above reference datum (m)
$\omega$	vertical velocity component in sigma coordinate system ( $\text{s}^{-1}$ ).

The discretized set of equations is solved on a staggered Arakawa B grid using an Alternating Direction Implicit method [Stelling, 1984; Leendertse, 1987] by specifying boundary conditions for the bed (quadratic friction law), free surface (wind stress), lateral boundaries (water level, currents, and/or discharges) and closed boundaries with free-slip conditions at the coast.

### 3.2. Wave model

Wind-generated waves are computed by the spectral wind wave model SWAN [Booij et al., 1999; Booij et al., 2004; Holthuijsen et al., 1993]. SWAN simulates the evolution of wave action density ( $N = E/\sigma$ , where  $E$  is the variance density and  $\sigma$  the intrinsic radian frequency) using the action balance equation (eq. 6), taking into account propagation in geographical space, depth- and current-induced refraction, the shifting of

the intrinsic radian frequency due to variation in mean current and depth, and various source terms (eq. 7):

$$\frac{\partial N}{\partial t} + \nabla_{x,y} \cdot [(\vec{c}_g + \vec{U})N] + \frac{\partial}{\partial \theta}(c_\theta N) + \frac{\partial}{\partial \sigma}(c_\sigma N) = \frac{S_{tot}}{\sigma} \quad (6)$$

$$S_{tot} = S_{in} + S_{wc} + S_{nl4} + S_{bot} + S_{brk} + S_{nl3} \quad (7)$$

In which:

$\theta$  direction space ( $^\circ$ )

$\vec{U}$  ambient current (m/s)

$c_g$  linear wave group velocity (m/s)

$c_\sigma, c_\theta$  propagation velocity in direction and frequency space(m/s)

The transfer of wind energy to the waves ( $S_{in}$ ), the dissipation of wave energy due to whitecapping ( $S_{wc}$ ), and the nonlinear transfer of wave energy due to quadruplet (four-wave) interactions ( $S_{nl4}$ ) are typical deep-water wave model components. In shallow water, additional terms include the dissipation due to bottom friction ( $S_{bot}$ ), depth-induced breaking ( $S_{brk}$ ), and nonlinear triad (three-wave) interaction ( $S_{nl3}$ ).

For use in SWAN, current information is converted from the three-dimensional flow field produced by the hydrodynamic model to a representative two dimensional flow field. By default, the top-layer of the three-dimensional flow field, given by (eq. 8), is used for this purpose. Alternatively, the depth-averaged velocity (eq. 9) can be applied. In strongly stratified flow conditions such as present at MCR, these approaches may give vastly different results and can be rather inaccurate. To better represent the influence of a

depth-varying current field on the wave field, the use of the averaging method of *Kirby and Chen* [1989], given by (eq. 10), was investigated. This expression, first applied to the Columbia River by *Lesser et al.* [2005], weights the magnitude of the current at a particular depth with the orbital velocity of a spectral component with wave number  $k$  at that same depth. For a stratified current profile, higher frequency components, whose orbital velocities are restricted to the upper layers of the water column, would therefore have a higher effective current compared to depth-averaged values, whereas low-frequency components are expected to yield results close to the depth-averaged values.

$$\vec{U}(x, y) = \vec{V}(x, y, 0) \quad (8)$$

$$\vec{U}(x, y) = \frac{1}{d} \int_{-d}^0 \vec{V}(x, y, z) dz \quad (9)$$

$$\vec{U}(x, y) = \frac{2k}{\sinh 2kd} \int_{-d}^0 \vec{V}(x, y, z) \cosh[2k(z + d)] dz \quad (10)$$

Here the impact of wave-orbital weighting is assessed by applying a single spectral mean wave number in (eq. 10) to represent the wave field, which produces a single weighted current field. The spectral mean wave number is computed by (eq. 11):

$$\tilde{k} = \frac{\int_0^{2\pi} \int_0^{\infty} kE(\sigma, \theta) d\sigma d\theta}{\int_0^{2\pi} \int_0^{\infty} E(\sigma, \theta) d\sigma d\theta} \quad (11)$$

In turn, the hydrodynamic and sediment transport models include the effect of waves on the instantaneous flow and transport. The following processes are included in the form of additional terms in the Reynolds and sediment transport equations: (a) radiation stresses, computed using the energy dissipation analogy of *Dingemans et al.* [1987], with the resulting forces distributed in the vertical over the breaking wave height,

(b) bed shear stresses, following the wave-current interaction model of *Fredsoe* [1984], (c) Stokes drift contributions to the Eulerian velocities, (d) wave-energy production and dissipation terms to the  $K-\varepsilon$  turbulence model, and (e) wave streaming [*Walstra et al.*, 2000].

### ***3.3. Application to the MCR field case***

#### ***3.3.1 Hydrodynamic model***

Grid schematization for any numerical model is a tradeoff between computational time and processes to be modeled. Grid resolution and time step should be sufficient to capture the phenomena of interest, but still allow efficient and accurate computations. At the MCR, important processes include ocean tides, waves, wind driven flows, estuarine circulation and their interactions. To accurately capture these processes, domain-decomposition was used to couple three well-structured, orthogonal curvilinear grids for the ocean, estuary and river domain (Figure 6). Grids are aligned along the land boundaries to improve numerical representation of the grid for the flow solver. The ocean domain has a maximum grid-size of  $2 \text{ km}^2$  along its seaward boundaries, and is refined towards the MCR. In the entrance, a horizontal resolution of 100 to 200 m is used to represent the jetties, navigation channel, and shoals. As the interaction of tidally-induced and density-driven flow is known to play an important role in the residual flow and sediment transports, it is crucial to capture the main features of the estuarine circulation accurately. A time step of 15 seconds results in a courant number below 10 for tidal wave propagation (sensitivity testing by running smaller time steps did not alter results). In the model, a 20-layer vertical grid schematization of the sigma layers ensures an adequate

feedback between salinity and the flow structure, accurately resolving the mixing of freshwater river discharge and saline sea water that drives complex estuarine circulations. Although the results presented here use a 20 layer vertical grid schematization, sensitivity testing revealed that near identical results can be obtained with a carefully selected 9 layer distribution. The  $K-\epsilon$  model, with default settings, was used as turbulence closure model. Corrections of artificial vertical diffusion errors due to steep bed gradients were accounted for [*Stelling and van Kester, 1994*]. The river domain is depth-averaged, because its primary purpose is to extend the model to the U.S. Geological Survey river gauging station at the Beaver Army Terminal near Quincy (OR), 86 km upstream from the mouth. Tidal energy extends beyond this location, but observed hourly flow data (water level and discharges) provides accurate upstream boundary conditions for the model (Figure 3b).

An initial estimate of the ocean boundary values was obtained from a regional scale model [*Lesser, 2009*] forced by the GOTOO.2 global tidal model estimates [*Ray, 1999*]. The calibrated main tidal constituents (Table 2) were imposed on the western boundary of the MCR ocean domain. The northern and southern boundaries were defined as zero-velocity Neumann boundaries (no alongshore water level gradient) which allow for the undisturbed propagation of alongshore currents out of the domain [*Roelvink and Walstra, 2004*]. Applying the Neumann boundaries is especially important for internally generated currents (e.g. due to wave breaking or density differences) that are difficult to predict and impose as boundary conditions without direct observations. A salinity value of 33 ppt. is prescribed on all open-sea boundaries. Although the seaward boundaries are located outside the direct sphere of inlet influence, the Columbia River plume often

extends beyond its seaward and northward limit [Hickey and Banas, 2003; Hickey et al., 2005]. An underlying assumption in these model simulations is that the buoyancy field at MCR is dominated by salinity, which is largely controlled by the known input of river water to the system, and the mixing of the river with the offshore waters [Horner-Devine, 2008]. Surface heat and freshwater heat fluxes were not considered as realistic treatment of temperature variations related to upwelling and downwelling and the effects on MCR circulation are not possible with the present boundary conditions. For simulations focusing on detailed plume dynamics the model would need to be coupled to a larger-scale domain to obtain a more realistic boundary forcing of the ocean circulation, density and temperature.

On the free surface, wind is implemented as a uniform shear stress, based on the wind data available from the nearby NDBC wave buoy 46029, and included in the momentum equations. Wind stress magnitudes are computed by,

$$\left| \overline{\tau}_s \right| = \rho_a C_d U_{10}^2 \quad (12)$$

Wherein  $\rho_a$  is the density of air ( $\text{kg/m}^3$ ),  $U_{10}$  the wind speed 10 m above the free surface (m/s) and  $C_d$  the wind drag coefficient. Wind speed dependent drag coefficients are defined accordingly,

$$C_d = C_d^A \left( C_d^B - C_d^A \right) \frac{U_{10} - U_{10}^A}{U_{10}^B - U_{10}^A} \quad (13)$$

With values for  $U_{10}^A = 0$  m/s,  $U_{10}^B = 100$  m/s, for  $C_d^A = 0.0025$  and  $C_d^B = 0.0289$ .

The bed stress ( $\overline{\tau}_b$ ) is modeled as a quadratic friction based on the magnitude of the Eulerian velocity in the first layer above the bed ( $\overline{u}_b$ ),

$$\overline{\tau}_b = \frac{g\rho_0\overline{u}_b|\overline{u}_b|}{C_{2D}^2} \quad (14)$$

With  $C_{2D}$  being the 2D- Chézy coefficient (based on calibration of water levels, see section 4.1).

The underlying model bathymetry is based on measurements provided by the USACE (Portland District) that were reconstructed from 2002-2004 data from the latest available National Ocean Service (NOS) data sets. These data were interpolated to a Washington State Plane 83 horizontal datum and the NGVD 29 vertical datum (Figure 2). Lidar elevation observations (2005) were used to schematize the intra- and supra-tidal shoal areas in the estuary in detail. These shoal complexes are essential to properly model the tidal storage and propagation in the estuary. Depending on the resolution of available observations, depth measurements were triangularly interpolated (low sample resolution) or grid-cell averaged (high sample resolution) to the curvilinear grid.

### 3.3.2 Wave model

The SWAN wave model version 40.72ABCDE was applied in third-generation mode. Deep water physics were modeled using the combination of wind input ( $S_{in}$ ) and saturation-based whitecapping ( $S_{wc}$ ) as proposed by *Van der Westhuysen* [2007]. Quadruplet nonlinear interaction ( $S_{nl4}$ ) was modeled using the Discrete Interaction Approximation (DIA) of *Hasselmann et al.* [1973a]. The shallow water source terms

include triad nonlinear interaction ( $S_{nl3}$ ) according to *Eldeberky* [1996] and bottom friction ( $S_{bot}$ ) according to *Hasselmann et al.* [1973b], both with their default settings in SWAN. For depth-induced breaking ( $S_{brk}$ ), the bi-phase breaker model of *Van der Westhuysen* [2010] was applied, with the parameter settings proposed by *Van der Westhuysen* [2009].

The curvilinear wave grid is based on the sea domain hydrodynamic grid (Figure 6). The offshore boundary extends to the location of the NDBC -46029- wave buoy. The directional spectrum observations from this buoy were applied as spatially constant, but time-varying boundary conditions. Spatially constant boundary conditions are justified given the high correlation between the Columbia River buoy and Grays Harbor buoy (NDBC buoy 46211) located some 75 km to the north. At the lateral boundaries, the specification of a uniform wave condition introduces some errors in the nearshore area due to water-depth restrictions. By using a slightly larger wave grid than hydrodynamic grid, these disturbances are damped before the flow model is reached and therefore do not affect the local model results at the MCR. The MCR jetties are implemented as non-penetrable obstacles (transmission coefficient 0). The default gradient based convergence criteria for relative change of wave height and local mean wave period have been applied. In addition, a small degree of under-relaxation ( $\alpha = 0.001$ ) was applied to improve the convergence behavior in the presence of strong opposing currents at the mouth (*van der Westhuysen and Elias, 2010*).

The hydrodynamic and wave models are run in so-called quasi-nonstationary mode. This involves a two-way coupling (10-minute intervals) of a nonstationary hydrodynamic calculation in combination with stationary wave model simulations. Every

10 minutes during the hydrodynamic simulation time SWAN is activated, and then performs a stationary simulation, using the corresponding measured wave spectra, and the corresponding water levels, currents and bed levels provided and computed by the hydrodynamic model, as boundary conditions.

#### Chapter 4: MODEL RESULTS

A robust model calibration requires synoptic data capturing as many processes as possible over a range of forcing conditions. The ultimate goal is to use the MGT dataset and numerical model to understand sediment transport patterns and processes at the MCR. However, before such assessment can be made, we need to ensure that the model captures the essentials of the underlying waves and currents. The hydrodynamic model skill is evaluated using the ‘index of agreement’ or skill as proposed by *Willmott* [1981]:

$$Skill = 1 - \frac{\sum (X_{Model} - X_{Obs})^2}{\sum (|X_{Model} - \bar{X}_{Obs}| + |X_{Obs} - \bar{X}_{Model}|)} \quad (15)$$

where  $X$  and  $\bar{X}$  are time-series and time-average of the selected variable. Skill varies between 0 (complete disagreement) and 1 (perfect agreement). The Willmott skill has been used by *Warner et al.* [2005] and *Liu et al.* [2009b] to quantify model performance in the Hudson and Columbia River estuary respectively. The advantage of model skill is that it is dimensionless so a comparison over multiple parameters can be made.

The predictive ability of the wave model was determined on the basis of relative bias (16), scatter index (17), and bias-corrected scatter index scores (18), which were computed for the significant wave height ( $H_{m0}$ ), the mean period ( $T_{m01}$ ) and the deep water steepness parameter ( $H_{m0}/L_0 = 2\pi H_{m0}/gT_{m0}^2$ ). These measures are defined respectively as

$$\text{Rel. bias}_X = \frac{BIAS_X}{\frac{1}{N} \sum_{i=1}^N X_{Obs}^i} \quad (16)$$

$$SI_X = \frac{\sqrt{\frac{1}{N} \sum_{i=1}^N (X_{Model}^i - X_{Obs}^i)^2}}{\frac{1}{N} \sum_{i=1}^N X_{Obs}^i} \quad (17)$$

$$BCSI_X = \frac{\sqrt{\frac{1}{N} \sum_{i=1}^N (X_{Model}^i - X_{Obs}^i - BIAS_X)^2}}{\frac{1}{N} \sum_{i=1}^N X_{Obs}^i} \quad (18)$$

With

$$BIAS_X = \frac{1}{N} \sum_{i=1}^N (X_{Model}^i - X_{Obs}^i) \quad (19)$$

#### 4.1 Tidal water levels

The 10 main tidal constituents were imposed on the western boundary of the MCR ocean domain and explain 99% of the ocean sea-level variance (Table 2). Towards and into the Columbia River, the baroclinic ocean tides are modified. These modifications result from bed friction on the relatively shallow ebb-tidal delta, and interactions with additional forcing mechanisms such as the buoyant plume (density gradients), wind and wave stresses. As a first step the constituents were corrected with

the local water level measurements taken at the MGT. This correction yielded amplitude corrections of 0 to 5% and phase corrections between 1 and 9 degrees. Secondly, water level data for representative stations distributed evenly over the estuary (Astoria, Skamokawa and Beaver Army Terminal, see Table 1 and Figure 2 for locations) were used to verify the correct tidal propagation in the estuary. The observed amplitude variations between the stations reveal the changing tidal wave shape as it propagates through the estuary. The observations illustrate that initially towards Astoria, the mean tidal range increases due to the funnel shape of the lower estuary. Upstream of Astoria, towards Skamokawa and Beaver, tidal modulation reduces due to the dominance of bed friction and opposite-directed river flow. The goodness of fit of the computed free surface was determined by performing harmonic tidal analysis on both the computed and observed water levels over synoptic time frames using the *t\_tide* toolbox [Pawlowicz *et al.*, 2002].

Initial simulations using constant bottom drag coefficients showed poor skill in reproducing the upper-estuary tidal propagation between Astoria and Skamokawa. An improved schematization of the major tidal flats and careful reconstruction of the channels upriver of Astoria, to accurately model storage volume and propagation on the relatively coarse grid, significantly improved the results. This highlights the importance of the bathymetry (and topography) in determining the accuracy of the model. To first order, the model conserves water mass; Thus, it is critical that: (1) an accurate combined bathymetry and topography map is present, (2) the model resolves the salient features, and (3) the model must employ numerical approaches and gridding schemes that are efficient enough to allow the required resolution. The sensitivity of the tidal propagation

was examined for a range of Manning (0.02, 0.0225, 0.0275 and 0.030) and Chézy (55, 60, 65 and 70  $\text{m}^{1/2}/\text{s}$ ) roughness coefficients. Using constant values for the Chézy bed roughness coefficient of 61  $\text{m}^{1/2}/\text{s}$  in the ocean domain, and lower values of 55  $\text{m}^{1/2}/\text{s}$  and 50  $\text{m}^{1/2}/\text{s}$  in the estuary and river domain yielded acceptable accuracy. Lower Chézy values upriver are consistent with the finding of *Giese and Jay* [1989] and are attributed to the lower effective drag coefficients in the stratified part of the system.

After calibration, the five major constituents ( $M_2$ ,  $K_1$ ,  $S_2$ ,  $O_1$ ,  $N_2$  and  $P_1$ ) show good skill at the calibration station MGT4 (Table 3 and Figure 7, top panel), while in the estuary amplitude errors of the major constituents are generally below 0.05 m, phase differences within 10 degrees, and model skill decreases from 0.99 at MGT 4 and Astoria to 0.96 at Beaver. Fine-tuning of the model settings by applying spatially variable bed roughness and increased grid resolution to resolve variations in bedform size and spacing in the estuary may improve the tidal predictions further, but was not attempted here.

## 4.2 *Salinity*

The estuarine salinity structure is a result of the interplay between the buoyancy flux from riverine inflow, advection by tides and the estuarine circulation, and mixing. Early field observations by *Hughes and Rattray* [1980] suggest that over half the up-estuary salt flux can be due to tidal pumping, with the remainder due to gravitational circulation. Accurate numerical predictions of the salinity field therefore depend critically on the accurate modeling of tidal and sub-tidal flow, as well as the accuracy of the turbulence closure parameterization for mixing of momentum and salt. An extensive elaboration on the importance of the turbulence closure schemes for estuarine dynamics

was addressed by *Warner et al.* [2005] using the ROMS model [*Shchepetkin and McWilliams*, 2005] and not repeated here. In this study it was found that the  $K-\epsilon$  model with default settings of eddy viscosity and diffusivity ( $1 \text{ m}^2/\text{s}$  and  $1 \times 10^{-6}$  for horizontal and vertical viscosity and diffusivity respectively) yielded good agreement in tidal monthly spring-neap variations in MGT4 (Figure 7d). The hydrodynamic model results were compared to estuary data collected at the SATURN observation stations red26, dsdma, grays, coaof and cbnc3. Relatively good skill is obtained in and near the MCR at stations MGT 3 and MGT 5, red26 and dsdma (Table 4). Perfect agreement between model and measurement is not expected as the response of the plume to coastal forcing is not included in the present model [*Chawla et al.*, 2008]. In general, skill values in the estuary decrease upstream (Table 4). Mid-estuary skill ranges between 0.83 and 0.86 at the stations of grays and coaof. Towards the upstream limits of salinity intrusion (cbnc3) skill reduces to 0.69. However this skill is still a confirmation that the upper limits of salinity intrusion are modeled well, and in agreement with the observations. The increasing discrepancies between model and observations must at least partly be attributed to model inaccuracies in hydrodynamics and vertical turbulent mixing due to the coarse model schematization, and errors in bathymetry. Skills scores are comparable to extensively calibrated and validated hydrodynamic models for the MCR such as presented in *Liu et al.* [2009a; 2009b].

### **4.3 Flow**

The MCR is known to exhibit strong along-channel, lateral and vertical variations in the flow fields from the complex interaction of friction, Coriolis force, channel

curvature and topography [*Cudaback and Jay, 2000; Cudaback and Jay, 2001*]. Model calibration and validation of flow with a limited number of observation stations is not trivial due to flow variability partially from flow interaction with local bathymetry. As a first step, we therefore qualitatively compare the modeled flow patterns (Figure 8) to existing knowledge. Model simulations show ocean residual flows predominantly to the south, consistent with the wind and wave direction during summer months (Figure 8c-d). Near the MCR currents increase strongly as flow is funneled through the entrance channel (Figure 8a-b). Areas of flow convergence and divergence roughly correlate with areas of strong bathymetric gradients. For example flow acceleration at the jetty tips is reflected in the form of large scour holes.

Modeled ebb currents are strongest in the central channel (Figure 8). Currents over the northern shoal are about half the speed of central-channel currents (Figure 8: MGT1 versus MGT5). The modeled surface outflow is stronger on the north side of the thalweg, while the inflow is shifted more to the channel axis. This asymmetry probably results from the forces of channel curvature and Coriolis that reinforce each other during ebb but are in opposition during flood. Also the upstream channel bifurcation (see Figure 2) and the interaction with the jetty tips are known to play an important role in the spatial flow variability. Consistent with observations, the southern fork of the channel bifurcation is governed by a net outflow. Blockage of the flood by a dominant outflow along the south side tends to push the inflow more northward. This strong lateral shear in estuarine along-channel transport with net landward transport of water and salt prevailing along the north side of the estuary, and a net seaward transport along the south side is a well-documented feature [*Hughes and Rattray, 1980; Jay and Smith, 1990*]. Validity of

the estuarine flow can further be inferred from the correspondence in salinity values (Table 4). The estuarine salinity structure is a result of the interaction between the buoyancy flux from riverine inflow, advection by tides and the estuarine circulation, and mixing. It has been shown that salinity intrusion is inversely dependent on tidal velocity [Geyer *et al.*, 2000]. Model skill ranges from 0.86 to 0.69 in the mid-estuary stations (grays, coaof and cbnc3; Table 4) near the upstream limits of salinity intrusion, indicate that the model representation of estuarine circulation was adequate.

A quantitative analysis of the model results is based on comparison of flow time-series (Figure 7 and 8), tidal ellipses (Figure 9) and residual flow distributions (Figure 10). The simulated velocities for MGT 1-5 were analyzed in the same manner as the observations. Synoptic time series of observational and model data were compiled, and the model data was linearly interpolated onto the corresponding ADCP bin-depths. Depth-averaged velocities were determined by averaging the ADCP bins between MLW and the bed. Principal axis decomposition was performed on the measured and modeled depth-averaged flow, and on the flow in the individual bins to determine major and minor components. Similar to the sea level variations, the along-channel (major) velocities are dominated by the semidiurnal tide with distinct spring-neap variations. Observed and modeled depth-averaged velocity magnitudes approach 1.5 m/s during spring flood tides and exceed 2.0 m/s during spring ebb. Model skill, ranges between 0.92 and 0.99 for the middle and bottom bins, with errors increasing towards the surface (Table 5). The top layer velocities are difficult to model due to the presence of waves, the buoyant plume, spatially variable winds, the relatively coarse vertical model schematization and limited data availability (only during flood).

The correspondence in measured and modeled flow ellipses illustrates that the model is able to capture the across channel variations in flow (Figure 9). In general, the flow velocities in the central part of the channel (MGT3) are reproduced more accurately than flow along the channel banks. The rotational character and a west-northwest orientation of the MGT 1 tidal ellipse display the sheltering effect of Jetty A on the local flow. The model reproduces the main direction but tends to over predict the bottom and mid-depth flow magnitudes at stations MGT 1 and MGT 5. Largest directional differences are observed at MGT 2 (top), and MGT 4 and MGT 5. A mismatch between model bathymetry and actual bathymetry present during the experiment as indicated in the observed depths of the stations might play a role. Flow magnitudes in the bottom layers of stations MGT 1 - 4 are accurately reproduced. The modeled mean flow shows the typical characteristics of stratification induced two-layer flow with a net outflow in the upper part of the profile, and inflow near the bottom (Figure 10, left). The modeled residual and mean peak ebb and flood flow accurately represent the observations (Figure 10, left and right respectively). The left-hand panel of Figure 10 approximates the transect-averaged, residual flow by averaging the individual MGT observations and corresponding model output (reference simulation). Results are presented as a station averaged flow, plotted over the relative depth wherein 0 is MSL and -1 the bed (the individual stations show similar results). Both the residual flow magnitude and the transition from seaward flow in the upper part of the profile and landward flow near the bed, typical for estuarine circulations, are well reproduced (Figure 10, left). There also exists excellent agreement between measured and observed (average) maximum ebb and flood peak velocities (Figure 8 bottom and the right panel of Figure 10). The subsurface

flood and ebb maxima, and the strong shear in velocities between bottom and surface bins are well reproduced.

We examined the sensitivity of the model to the various forcing processes (density, wind, waves). The importance of the density-driven circulation was investigated by running the model with a saline river discharge. The results reveal that in the absence of density gradients a near-uniform outflow ( $\sim 0.1$  m/s) prevails. Density gradients introduce the observed and modeled reversal of the mean flow at the bed and augment mean and peak flow in the upper half of the water column. *García Berdeal et al.* [2002] and *MacCready et al.* [2009] point to the importance of wind on the Columbia River Plume dynamics. In the model, contributions of wind and waves on peak ebb and flood flow are minor with a 1 to 10% increase of the residual outflow near the surface and similar decrease in inflow near the bed (Figure 10). The limited wind and wave influence is due to the calm conditions encountered during the MGT experiment.

#### **4.4 Waves**

Validation of the wave model SWAN focuses on the process of wave-current interaction and bottom friction. *Olabarrieta et al.* [2011] showed the importance of wave-current interactions in the nearby Willapa Bay. The measured wave height time-series of Figure 4b clearly illustrate the importance of wave-current interactions in the MCR as during opposing ebb tides waves nearly double in height. In general the wave model tends to underestimate the larger wave heights during peak ebb (Figure 7). This is clearly evident between 03/08 and 10/08 and linked to the discrepancy in modeled velocities. The sensitivity of the wave-current interaction and related amplified wave heights is

clearly illustrated in Figure 12. The MGT measurements are at the edge of the amplified wave-height zone and small deviations can lead to significant offsets.

As described in section 3.2, the standard version of the Delft3D-SWAN uses the top layer of the three-dimensional current field as the representative two-dimensional current field in SWAN (eq. 8). Under highly-stratified conditions such as in the MCR this approach may not be valid. Hence two alternative approaches for integrating the current profile are considered here, namely taking the depth-averaged velocities (eq. 9) or the wave-weighted approach of *Kirby and Chen* [1989] given by (eq. 10).

Figure 11 presents the corresponding scatter plot using all of the MGT data compared to the model results. Depth-averaging of the current (eq. 9, center column) yields a smaller bias-corrected scatter index in  $H_{m0}$  than the top-layer approach (eq. 8, left-hand column), 0.197 versus 0.212, but increases the negative bias from -0.06 to -0.126. Especially higher wave heights appear to be underestimated. With this approach, both the scatter and the bias of the mean period increase. The scatter in the mean steepness parameter  $H_{m0}/L_{m0}$  also increases (0.091 to 0.119), but, due to the lower mean periods, the bias is reduced from -0.069 to -0.017. The right-hand column presents the results of the simulation with wave orbital-weighted velocities (eq. 10), the physically most realistic of the three averaging options. Using this approach, the bias-corrected scatter of  $H_{m0}$  is somewhat reduced (from 0.0197 to 0.0193), and so is the bias of the mean steepness  $H_{m0}/L_{m0}$ . The statistics of  $T_{m0}$  are relatively unchanged. The negative bias in  $H_{m0}$  is slightly increased from -6% to -7%. The orbital-averaged method yields somewhat better accuracy than both the top-layer and simple depth-averaged methods. Because this approach also provides a better representation of the underlying physics of

wave-current interaction, the wave orbital-averaged approach (eq. 10) was taken as the calibration result.

Although not fully evident in the scatter plots, the importance of the flow on wave attenuation is clearly illustrated in Figure 12. For one selected time step during representative ebb, the right panels of Figure 12 show the resultant 2DH current field (input to SWAN) and the left panels the  $H_{m0}$  fields for the three current averaging approaches. It can be seen that the  $H_{m0}$  is significantly increased in the mouth due to the ebb flow. The simulation with depth-averaged currents yields the lowest effective currents and wave heights. It is, however, interesting to note that the plume mostly affects the wave field offshore of the MGT stations, so that its impact is much attenuated in the computed time series at MGT4.

In the results presented above, a wave bottom friction coefficient  $C_{f,JON} = 0.067 \text{ m}^2\text{s}^3$  was used, which is the default value in SWAN for wind sea conditions, based on *Bouws and Komen* [1983]. However, considering that the wave energy propagating through the domain is mainly swell from the offshore, a lower value of  $C_{f,JON} = 0.038 \text{ m}^2\text{s}^3$  (swell default, based on *Hasselmann et al.*, 1973b) may be more appropriate. In addition, *Van Vledder et al.* [2010] argue that this lower value of  $C_{f,JON}$  is appropriate under both wind sea and swell conditions. Using the lower  $C_{f,JON}$  an improvement can be seen in the results for  $H_{m0}$ , with a reduction in the negative bias from -7% to -4%. The bulk statistics for  $T_{m0}$  and the steepness parameter  $H_{m0} / L_{m0}$  show only small differences (Table 6).

From the above, the model variant featuring wave-weighted current velocities and a bottom friction coefficient of ( $C_{f,JON} = 0.038 \text{ m}^2\text{s}^3$ ) is considered to be the most accurate

of those considered here, and is applied with these settings in combination with the hydrodynamic model.

## **Chapter 5: CONCLUSIONS AND RECOMMENDATIONS**

### ***5.1. Conclusions***

A coupled hydrodynamic and wave model for the Mouth of the Columbia River (MCR) based on the Delft3D modeling system was constructed to allow state-of-the-art sediment transport modeling in this dynamic estuary entrance (see Part II). The following conclusions can be drawn from the results of this study:

1. The Mega Transect (MGT) measurements provide a valuable dataset for model validation.
2. The measured conditions are typical for summer conditions at MCR.
3. The MCR model presented here is able to simulate the dominant features of the observed tidal flow, salinity and wave fields, which are all important to the accurate modeling of sediment transport.
4. A calibration of the bed roughness in combination with default settings of the flow model yielded good agreement in modeled surface elevation, flow and salinity at the MCR and through the estuary.
5. Current velocity profiles in the MCR are highly stratified. Of the three methods considered for representing these profiles in the wave model with a single value - top layer, depth-averaged or wave orbital averaged – the latter, proposed by *Kirby and Chen* [1989], is considered the most realistic for the MCR. Applying this method using a single mean wave number yields some improvement in results relative to simulations using the top layer. The performance of the full expression,

- in which an effective current field is computed for each spectral component, should be investigated here.
6. The use of a lower bottom friction coefficient ( $C_{f, JON} = 0.038 \text{ m}^2\text{s}^3$ ) improved results of  $H_{m0}$ , especially during ebb, relative to those obtained with  $C_{f, JON} = 0.067 \text{ m}^2\text{s}^3$  without deterioration in the mean period  $T_{m01}$ .
  7. Sensitivity studies shows that, in the absence of density-driven circulation, a near-uniform seaward flow ( $\sim 0.1 \text{ m/s}$ ) prevails below MLW. Density gradients introduce a reversal of the mean flow at the bed which will be critical to sediment transport calculations and augment mean and peak flow in the upper half of the water column.
  8. Contributions of wind and waves on residual flow and peak ebb and flood flow were minor due to the calm conditions encountered during the summer MGT experiment. This implies that sediment transport during calmer summer conditions is controlled by density stratification and is likely net landward due to the reversal of flow near the bed. During winter conditions, when wind and waves are larger and more important, net circulation may be different and the control on sediment transport more complicated. These implications for sediment transport are the central focus of related studies which will be published in future work.

## ***5.2. Recommendations***

The correspondence between observed and modeled hydrodynamics illustrates that the model is well capable of reproducing the hydrodynamic behavior of a dynamic estuary entrance, like the Mouth of the Columbia River, at least during summer

conditions. Especially the important density driven reversal of mean flow from outflow to inflow near the bed is well reproduced. This makes the presented model application a powerful tool to investigate hydrodynamics and associated sediment transports.

River discharges varies strongly throughout the year and the associated density fields are likely to fluctuate correspondently. The model should be run over a broad range of river conditions to investigate the effects of stratification on residual flow and sediment transport at the MCR. Similarly, wind and waves are known to vary seasonally and it is likely that sediment transport is wind and wave dominated during storm events, while density stratification is less pronounced. Running the model over a large range of coastal and river forcing conditions can identify the sediment transport magnitudes and patterns over long-term (year-averaged), thus supporting management of the estuary entrance.

Such events were however not present during the MGT observations. A broader range of validation and calibration is therefore essential. Recently added wave buoys on the ebb-tidal delta and nearshore measurements provide a more comprehensive validation dataset that should be included.

To improve model prediction in the ocean and MCR domain a detailed prescription of boundary conditions is needed to include large-scale coastal forcing such as upwelling and downwelling events. Large-scale ocean models are available to provide these boundaries. Density variations in the present model are only attributed to salinity, whereas additional parameters such as temperature should be included.

One important aspect is the importance of the current field on the waves. The most pronounced effects are observed seaward of the MGT, were measurements are

lacking. Measurements on a broader spatial scale are essential to further validate the model performance for wave current interaction.

### **Acknowledgements**

This work was carried out in cooperation between the US Geological Survey and Deltares. Funding for this study was provided by USGS Coastal and Marine Geology Program, USACE, NOAA, Deltares and the Dutch Centre for Water Management. We thank Giles Lesser for his original contributions to the MCR model, Hans Moritz for his leadership in obtaining the MGT data and Andrew Stevens for post-processing the MGT data.

## References

- Allan, J., and P. D. Komar (2000), Are Ocean Wave Heights Increasing in the Eastern North Pacific, *EOS Trans. AGU*, 81(47).
- Banas, N. S., P. MacCready, and B. M. Hickey (2009), The Columbia River plume as cross-shelf exporter and along-coast barrier, *Continental Shelf Research*, pp. 292-301, doi: 10.1016/j.csr.2008.03.011.
- Baptista, A. M. (2006), CORIE: The first decade of a coastal-margin collaborative observatory, paper presented at Oceans 2006, Inst. of Electr. And Electr. Eng., Boston, pp. 1-6.
- Baptista, A. M., Y. L. Zhang, A. Chawla, M. Zulauf, C. Seaton, E. P. Myers III, J. Kindle, M. Wilkin, M. Burla, and P. J. Turner (2005), A cross-scale model for 3D baroclinic circulation in estuary-plume-shelf systems: II. Application to the Columbia River. *Continental Shelf Research* 25, 935–972, doi: 10.1016/j.csr.2004.07.021,.
- Barnes, C. A., A. C. Duxbury, and B. A. Morse (1972), Circulation and selected properties of the Columbia River effluent at sea, in *The Columbia River Estuary and Adjacent Ocean Waters*, edited by A. T. Pruter and D. L. Alverson, pp. 41–80, University of Washington Press, Seattle, WA.
- Battelle, (2011), Final Independent External Peer Review Report Columbia River at the Mouth, Oregon and Washington, Major Rehabilitation Evaluation Report, Battelle, Columbus, OH, 87 pp.
- Booij, N., R. C. Ris, and L. H. Holthuijsen (1999), A third-generation wave model for coastal regions, Part I: Model description and validation, *Journal of Geophysical Research*, 104, C4, pp. 7649-7666, doi: 10.1029/98JC02622.
- Booij, N., I. G. Haagsma, L. H. Holthuijsen, A. T. M. M. Kieftenburg, R. C. Ris, and A. J. v. d. Westhuysen (2004), SWAN Cycle III version 40.41 USER MANUAL, Delft University of Technology, Delft, the Netherlands.
- Bottom, D. L., C. A. Simenstad, J. Burke, A. M. Baptista, D. A. Jay, K. K. Jones, E. Casillas, and M. H. Schiewe (2005), Salmon at river's end: The role of the estuary in the decline and recovery of Columbia River salmon. *U.S. Dept. Commer., NOAA Tech. Memo, NMFS1168 NWFSC-68*, 246 pp. ,
- Bouws, E., and G. J. Komen (1983), On the balance between growth and dissipation in an extreme, depth limited wind-sea in the southern North Sea. *Journal of Physical Oceanography*, 13, pp. 1653-1658, doi: 10.1029/98JC02622.

Buisman, M. C., C. R. Sherwood, A. E. Gibbs, G. Gelfenbaum, G. Kaminsky, P. Ruggeriero, and J. Franklin (2003), Regional Sediment Budget of the Columbia River Littoral Cell, USA, Analysis of Bathymetric- and Topographic-Volume Change, *Open-File Report 02-281*, US Geological Survey, Calif.

Burla, M., A. M. Baptista, Y. Zhang, and S. Frolov (2010), Seasonal and inter-annual variability of the Columbia River plume: A perspective enabled by multi-year simulation databases. *Journal of Geophysical Research*, 115, C00B16, doi: 10.1029/2008JC004964.

Byrnes, M.R., Griffiee, S.F., Moritz, H.R., (2007). Engineering Activities Influencing Historical Sediment Transport Pathways at the Columbia River Mouth, WA/OR, paper presented at Coastal Sediments '07, ASCE, New Orleans, Louisiana, doi: 10.1061/40926(239)138)

Casillas, E. (1999), Role of the Columbia River estuary and plume in salmon productivity. Paper presented at Ocean Conditions and the Management of Columbia River Salmon, Portland, OR.

Chawla, A., D. A. Jay, A. M. Baptista, M. Wilkin, and C. Seaton (2008), Seasonal variability and estuary-shelf interactions in circulation dynamics of a river-dominated estuary, *Estuaries Coasts*, 31, pp. 269 – 288, doi: 10.1007/s12237-007-9022-7.

Cudaback, C. N., and D. A. Jay (2000), Tidal asymmetry in an estuarine pycnocline: Depth and thickness, *Journal of Geophysical Research*, 105(26), pp. 237– 252, doi: 10.1029/2000JC900135.

Cudaback, C. N., and D. A. Jay (2001), Tidal asymmetry in an estuarine pycnocline: 2. Transport, *Journal of Geophysical Research*, 106(c2), pp. 2639 – 2652, doi: 10.1029/2000JC900151.

Deltares (2010), Delft3D-FLOW. Simulation of multi-dimensional hydrodynamic flows and transport phenomena, including sediments. *User Manual. Version: 3.14, revision 11214*, Deltares, Delft, the Netherlands.

Dingemans, M. W., A. C. Radder, and H. J. De Vriend (1987), Computation of the driving forces of wave-induced currents, *Coastal Engineering*, 11, pp. 539– 563, doi: 10.1016/0378-3839(87)90026-3.

Eldeberky, Y. (1996), Nonlinear transformations of wave spectra in the nearshore zone, Ph.D. thesis, Department of Civil Engineering and Geosciences, Delft University of Technology, Delft, the Netherlands.

Elias, E. P. L., D. J. R. Walstra, J. A. Roelvink, M. J. F. Stive, and M. D. Klein (2000), Hydrodynamic validation of Delft3D with field measurements at Egmond, paper presented at 27th ICCE, ASCE, New York.

- Elias, E. P. L., J. Cleveringa, M. C. Buisman, M. J. F. Stive, and J. A. Roelvink (2006), Field- and model data analysis of sand transport patterns in Texel Tidal inlet (the Netherlands), *Coastal Engineering*, 53(5-6), pp: 505-529, doi: 10.1016/j.coastaleng.2005.11.006,.
- Fredsoe, J. (1984), Turbulent boundary layer in wave-current interaction, *Journal of Hydraulic Engineering*, 110, pp. 1103-1120, doi: 10.1061/(ASCE)0733-9429(1984)110:8(1103).
- García Berdeal, I., B. M. Hickey, and M. Kawase (2002), Influence of wind stress and ambient flow on a high discharge river plume. *Journal of Geophysical Research*, 107(C9), doi: 10.1029/2001JC000932.
- Gelfenbaum, G., and G. M. Kaminsky (2010), Large-scale coastal change in the Columbia River littoral cell: An overview. *Marine Geology*, 273(1-4), pp. 1-10, doi: 10.1016/j.margeo.2010.02.007.
- Gelfenbaum, G., C. R. Sherwood, C. D. Peterson, M. D. Kaminsky, M. C. Buisman, D. C. Twichell, P. Ruggiero, A. E. Gibbs, and C. Reed (1999), The Columbia littoral cell: a sediment budget overview, paper presented at 4th ICCE, ASCE, Long Island, NY.
- Gerritsen, H., E. D. de Goede, F. W. Platzek, M. Genseberger, J. A. T. M. van Kester, and U. R.E (2007), Validation Document Delft3D-FLOW; a software system for 3D flow simulations. *Report X0356, M3470*, Deltares, Delft, the Netherlands.
- Geyer, W. R., J. H. Trowbridge, and M. M. Bowen (2000), The dynamics of a partially mixed estuary, *Journal of Physical Oceanography*, 30, pp. 2035–2048, doi: 10.1175/1520-0485.
- Giese, B. S., and D. A. Jay (1989), Modeling Tidal Energetics of the Columbia River Estuary, *Estuarine Coastal and Marine Science*, 29(6), pp. 549–571, doi: 10.1016/0272-7714(89)90010-3.
- Groeneweg, J., A. J. van der Westhuysen, G. P. van Vledder, S. Jacobse, J. Lanssen, and A. R. van Dongeren (2008), Wave modelling in a tidal inlet: Performance of SWAN in the Wadden Sea, paper presented at 31th Int. Conf. Coastal Eng., ASCE, Hamburg, Germany.
- Hamilton, P. (1990), Modeling salinity and circulation for the Columbia River estuary, *Prog. Oceanography*, 25(1-4), pp. 113–156.
- Hasselmann, D. E., M. Dunckel, and J. A. Ewing (1973a), Directional Wave Spectra Observed during JONSWAP 1973, *Journal of Physical Oceanography*, 10:88, pp. 1264–1280, doi: 10.1175/1520-0485(1980)010<1264:DWSODJ>2.0.CO;2.

Hasselmann, K., T. P. Barnett, E. Bouws et al. (1973b), Measurements of wind-wave growth and swell decay during the North Sea Wave Project (JONSWAP), *Ergänzungsheft zur Deutschen Hydrographischen Zeitschrift*, volume 8(12), 95 pp.

Hibma, A. (2004), Morphodynamic modeling of channel-shoal systems, 122 pp, Ph.D thesis, Department of Civil Engineering and Geosciences, Delft University of Technology, Delft, the Netherlands.

Hickey, B., S. Geier, N. Kachel, and A. MacFadyen (2005), A bi-directional river plume: The Columbia in summer. *Continental Shelf Research*, 25(14), pp. 1631–1656, doi: 10.1016/j.csr.2005.04.010.

Hickey, B. M. (1998), Coastal Oceanography of Western North America from the tip of 1253 Baja California to Vancouver Is, in *The Sea*, edited by K. H. Brink and A. R. Robinson, pp. 345–393, John Wiley and Sons Inc., New York.

Hickey, B. M., and N. Banas (2003), Oceanography of the Pacific Northwest coastal ocean and estuaries with application to coastal ecosystems. *Estuaries Coasts*, 26(48), pp. 1010– 1031, doi: 10.1007/BF02803360.

Hickey, B. M., R.M. Kudela, J.D. Nash, K.W. Bruland et al. (2010), River Influences on Shelf Ecosystems: Introduction and synthesis. *Journal of Geophysical Research*, 115(C00B17), doi: 10.1029/2009JC005452.

Hickey, B. M., L. J. Pietrafesa, D. A. Jay, and W. C. Boicourt (1998), The Columbia River plume study: Subtidal variability in the velocity and salinity fields, *Journal of Geophysical Research*, 103(C5), pp. 10339 – 10368, doi: 10.1029/97JC03290.

Hickson, R. E. (1936), Beach erosion at the mouth of the Columbia River, *Shore and Beach*, 4(4), pp. 147–150.

Holthuijsen, L. H., N. Booij, and R. C. Ris (1993), A Spectral Wave Model for the Coastal Ocean, paper presented at Proceedings of the 2nd International Symposium of Ocean Wave Measurement and Analysis, New Orleans.

Horner-Devine, A. R. (2008), The bulge circulation in the Columbia River plume, *Continental Shelf Research*, 29(1), pp. 234–251, doi: 10.1016/j.csr.2007.12.012.

Horner-Devine, A. R., D. A. Jay, P. M. Orton, and E. Spahn (2009), A conceptual model of the strongly tidal Columbia River plume, *Journal of Marine Systems*, 78(3), pp. 460-475, doi: 10.1016/j.jmarsys.2008.11.025.

Hsu, Y. L., J. D. Dykes, and R. A. Allard (2008), Validation Test Report for Delft3D. *Report NRL/MR/7320--08-9079*, Naval Research Laboratory, Oceanography Division, Stennis Space Center, MS.

- Hughes, R. P., and M. Rattray (1980), Salt flux and mixing in the Columbia River estuary, *Estuarine Coastal and Marine Science*, 10, pp. 479– 494.
- Jay, D. A., and J. D. Smith (1990), Circulation, density distribution and spring-neap transitions in the Columbia River Estuary, *Prog. Oceanography*, 25(81), 12 pp.
- Jay, D. A., B. S. Giese, and C. R. Sherwood (1990), Energetics and Sediment Process in the Columbia River Estuary, *Progr. Oceanog*, 25, pp. 157–174, doi: 10.1016/0079-6611(90)90004-L.
- Kaminsky, G. M., P. Ruggiero, B. C. Buisman, D. McCandless, and G. Gelfenbaum (2010), Historical evolution of the Columbia River littoral cell, *Marine Geology*, 273(1-4), pp. 96-126, doi: 10.1016/j. margeo.2010.02.006.
- Kirby, J. T., and T.-M. Chen (1989), Surface waves on vertically sheared flows: approximate dispersion relations, *Journal of Geophysical Research*, 94(C1), pp. 1013-1027, doi: 10.1029/JC094iC01p01013.
- Klein, M. D., E. P. L. Elias, M. J. F. Stive, and D. J. R. Walstra (2001), Modeling inner surf zone hydrodynamics at Egmond, The Netherlands, paper presented at 4th Int. Conf. on Coastal Dynamics '01, ASCE, Lund, Sweden.
- Leendertse, J. J. (1987), A three-dimensional alternating direction implicit model with iterative Fourth order dissipative non-linear advection terms. *Report WD-3333-NETH*, Rijkswaterstaat. the Hague, the Netherlands.
- Lesser, G. R., G. Gelfenbaum, and H. Moritz (2005), Wave-current interaction and its effect on sand transport at the mouth of a dynamic estuary. Mouth of the Columbia River, OR. , AGU fall meeting 2005, Abstract #H51D-0402, San francisco, Ca.
- Lesser, G. R., J. A. Roelvink, J. A. T. M. van Kester, and G. S. Stelling (2004), Development and validation of a three-dimensional morphological model, *Coastal Engineering*, 51, pp. 883-915, doi: 10.1016/j.coastaleng.2004.07.014.
- Lesser, G. R. (2009), An approach to medium-term coastal morphological modeling, Ph.D Thesis, UNESCO-IHE Institute for Water Education, Delft, the Netherlands.
- Liu, Y., M. P. MacCready, and B.M. Hickey (2009a), Columbia River plume patterns in summer 2004 as revealed by a hindcast coastal ocean circulation model, *Geophysical Research Letters*, 36(L02601), doi: 10.1029/2008GL036447.
- Liu, Y., P. MacCready, B. M. Hickey, E. P. Dever, P. M. Kosro, and N. S. Banas (2009b), Evaluation of a coastal ocean circulation model for the Columbia River plume in 2004, *Journal of Geophysical Research*, 114(C00B4), doi: 10.1029/ 2008JC004929.

- MacCready, P., N. S. Banas, B. M. Hickey, E. P. Dever, and Y. Liu (2009), A model study of tide- and wind-induced mixing in the Columbia River estuary and plume. *Continental Shelf Research*, 29, pp. 278-291, doi: 10.1016/j.csr.2008.03.015.
- Mikhailova, M. V. (2008), Hydrological and Morphological Processes in the Mouth Area of the Columbia River (United States) and Their Changes under the Impact of Large-Scale Hydro-engineering Works, *Water Resources*, 35(2), pp. 137–155, doi: 10.1134/S0097807808020024.
- Morgan, C. A., A. De Robertis, and R. W. Zabel (2005), Columbia River plume fronts: I. Hydrography, zooplankton distribution, and community composition, *Mar. Ecol. Prog. Ser.*, 299, pp. 19 – 31.
- Moritz, H. R., H. P. Moritz, J. R. Hays, H. R. Sumerell (2003), 100-years of shoal evolution at the Mouth of the Columbia River: impacts on channel, structures, and shorelines, paper presented at Coastal Sediments '03, East Meets West Productions, CD-ROM.
- Moritz, H. R., G. Gelfenbaum, G. M. Kaminsky, P. Ruggiero, J. Oltman-Shay, and D. J. McKillip (2007), Implementing Regional Sediment Management to Sustain Navigation at an Energetic Tidal Inlet, paper presented at Coastal sediments '07, USACE, New Orleans. Louisiana.
- Morris, B. J. (2001), Nearshore wave and current dynamics, Ph.D thesis. Naval Post Graduate School, Monterey, California.
- Mulligan, R. P., A. E. Hay, and A. J. Bowen (2008), Wave-driven circulation in a coastal bay during the landfall of a hurricane, *Journal of Geophysical Research*, 113(C05026), doi: 10.1029/2007JC004500.
- Mulligan, R. P., A. E. Hay, and A. J. Bowen (2010), A wave-driven jet over a rocky shoal, *Journal of Geophysical Research*, 115(C10038), doi: 10.1029/2009JC006027.
- Mulligan, R.P., Perrie, W., and Solomon, S. (2010). Dynamics of the Mackenzie River plume on the inner Beaufort Shelf during an open water period in summer. *Estuarine, Coastal and Shelf Sci.* (89), 214-220. doi: 10.1016/j.ecss.2010.06.010
- Orton, P. M., and D. A. Jay (2005), Observations at the tidal plume front of a high volume river outflow, *Geophysical Research Letters*, 32, doi: 10.1029/2005GL022372.
- Olabarrieta, M., J. C. Warner, and N. Kumar (2011), Wave-current interaction in Willapa Bay, *J. Geophys. Res.*, 116, C12014, doi:10.1029/2011JC007387
- Pawlowicz, R., B. Breardsley, and S. Lentz (2002), Classical tidal harmonic analysis including error estimates in MATLAB using T\_TIDE, *Computers and Geosciences*, 28(8), pp. 929-937, doi: 10.1016/S0098-3004(02)00013-4.

- Ray, R. (1999), A global ocean tide model from Topex/Poseidon altimetry: GOT99.2. NASA Tech Memo 209478, 58 pp, Nasa Center for AeroSpace Information, Hanover, MD.
- Roelvink, J. A., and D. J. R. Walstra (2004), Keeping it simple by using complex models, paper presented at 6th International Conference on Hydroscience and Engineering, Brisbane, Australia.
- Shchepetkin, A. F., and J. C. McWilliams (2005), The Regional Ocean Modeling System: A split-explicit, free-surface, topography following coordinates ocean model, *Ocean Modeling*, 9, pp: 347-404, doi: 10.1016/j.ocemod.2004.08.002.
- Ruggiero, P., G. M. Kaminsky, P. D. Komar, and W. G. McDougal (1997), Extreme waves and coastal erosion in the Pacific Northwest, paper presented at Waves '97 ASCE.
- Sherwood, C. R., and J. S. Creager (1990), Sedimentary Geology of the Columbia River Estuary, *Progr. Oceanog*, 25, pp: 15–79, doi: 10.1016/0079-6611(90)90003-K,.
- Sherwood, C. R., D. A. Jay, and R. B. Harvey (1990), Historical Changes in the Columbia River Estuary, *Progr. Oceanog*, 25, pp: 299–352, doi: 10.1016/0079-6611(90)90011-P,.
- Spahn, E. Y., A. R. Horner-Devine, D. A. Jay, J. Nash, and L. Kilcher (2009), Particle re-suspension in the Columbia River plume near field, *Journal of Geophysical Research*, doi: 10.1029/2008JC004986.
- Stelling, G. S. (1984), On the construction of computational methods for shallow water flow problems., Rijkswaterstaat communications, 35 pp, The Hague, the Netherlands.
- Stelling, G. S., and J. A. T. M. van Kester (1994), On the approximation of horizontal gradients in sigma co-ordinates for bathymetry with steep bottom slopes, *International Journal Numerical Methods In Fluids*, 18, doi: 10.1002/flid.1650181003.
- Styles, R. (2006), Application of a bottom boundary layer model in contrasting wave and current environments: Grays Harbor, Washington, *Journal of Waterway, Port, Coastal and Ocean Engineering*, 132(5), pp. 379–387, doi: 10.1061/(ASCE)0733-950X, 379-387.
- Sutherland, J., D. J. Walstra, T. J. Chester, L. C. Van Rijn, and H. N. Southgate (2004), Evaluation of coastal area modeling systems at an estuary mouth, *Coastal Engineering*, 51, pp. 119-142, doi: 10.1016/j.coastaleng.2003.12.003.
- Tillotson, K. J., and P. D. Komar (1997), The wave climate of the Pacific Northwest (Oregon and Washington): a comparison of data sources, *Journal of Coastal Research*, 13, pp. 440–452.

Van der Westhuysen, A. J. (2007), Advances in the spectral modeling of wind waves in the nearshore, Ph.D Thesis, Department of Civil Engineering and Geosciences, Delft University of Technology, Delft, the Netherlands.

Van der Westhuysen, A. J. (2009), Modeling of depth-induced wave breaking over sloping and horizontal beds., paper presented at Proceedings 11th International Workshop on Wave Hindcasting and Forecasting, Halifax.

Van der Westhuysen, A. J. (2010), Modeling of depth-induced wave breaking under finite depth wave growth conditions. *Journal of Geophysical Research*, 115(C01008), doi: 10.1029/2009JC005433.

van der Westhuysen, A.J., Elias, E.P.L. (2010), Validation of wave-current interaction modelling in the Western Scheldt and the Columbia River Mouth. Report, Deltares 1202120-004, Delft, the Netherlands, 157 pp.

Van Maren, D. S. (2004), Morphodynamics of a cyclic prograding delta: the red river, Vietnam, Ph.D Thesis, Utrecht University, Utrecht, the Netherlands.

Van Rijn, L. C. (1993), Transport of fine sands by currents and waves, *Journal of Waterway, Port, Coastal and Ocean Engineering*, 119(2), pp. 123-143.

Van Vledder, G. P., J. Groeneweg, and A. J. van der Westhuysen (2008), Numerical and physical aspects of wave modeling in a tidal inlet, paper presented at Proc. 31th Int. Conf. Coastal Eng, ASCE, Hamburg, Germany.

Van Vledder, G. P., M. Zijlema, and L. H. Holthuijsen (2010), Revising the Jonswap bottom friction formulation in wind-driven storm seas. , paper presented at Proceedings of the 32th Conference of Coastal Engineering, ASCE, Shanghai, China.

Walstra, D. J., J. A. Roelvink, and J. Groeneweg (2000), Calculation of wave-driven currents in a 3D mean flow model, paper presented at Proc. of 27th Conference on Coastal Engineering, ASCE, Sydney, Australia.

Ward, D. L. (1988), Case histories of corps breakwater and jetty structures. Report 6 North Pacific Division. Repair, Evaluation, maintenance and rehabilitation research program. *Report REMR-CO-3*, USACE, Waterways Experiment Station, Vicksburg (MS).

Warner, J. C., W. R. Geyer, and J. A. Lerczak (2005), Numerical modeling of an estuary: A comprehensive skill assessment, *Journal of Geophysical Research*, 110, doi: 10.1029/2004JC002691.

Wilmott, C. J. (1981), On the validation of models. *Physical Geography*, 2, pp. 184–194.

Zhang, Y. L., and A. M. Baptista (2008), SELFE: A semi-implicit Eulerian-Lagrangian finite-element model for cross-scale ocean circulation, *Ocean Modeling*, 21, pp. 71–96, doi: 10.1016/j.csr.2004.07.021.

Figure 1: The Columbia River is located in the Pacific Northwest coast of the United States, and forms part of the Columbia River Littoral Cell that spans 165 km of coastline between Tillamook Head (Oregon) to the south and Point Grenville (Washington) to the north. The Continental Shelf facing the MCR is 25 to 50 km wide with depths increasing to 150m.

Figure 2: MCR model bathymetry (2002-2004 data) and details of the MCR (insert). The MCR connects the lower Columbia River estuary to the Pacific Ocean. The asymmetric ebb-tidal delta protrudes 7 km seaward and 15 km alongshore and is dissected by a 17m deep navigational channel. The federal navigational channel is kept in depth and place by maintenance dredging and three major stone jetties: North Jetty, South Jetty and Jetty A. The North and South Jetty extend 3.5 km and 10 km seaward, respectively. Located slightly inward and normal to the channel axis, Jetty A was added in 1939 to further stabilize the shifting channel. Maximum depths of 25 to 25 m are observed at the Jetty tips. The main channel is aligned along the tips of North-Jetty and Jetty A. Clatsop spit forms a buffer between a major part of South Jetty and the channel. MGT1-5 indicates the tripod locations during the Mega Transect Experiment.

Figure 3: Overview of the forcing conditions during the timeframe of the MGT experiment (3 August – 9 September 2005). From top to bottom: (a) measured water levels at Astoria, (b) daily mean discharges at Beaver Army Terminal, (c, d, e, f) hourly values of wind speed ( $U_{10}$ ), significant wave height, direction and peak period from NDBC buoy 46029 (see Table 1 for location).

Figure 4: Time series of representative measurements for the MGT experiment at stations 4 and 5. From top to bottom: (a) water levels (MGT 4), (b) significant wave heights (MGT 4), (c) salinity (MGT 5), (d) depth-averaged velocity derived from averaging the ADCP bins (MGT 5), (e) orbital velocities (ADV, MGT 5), and (f) sediment concentrations at 1.3m above the bed for OBS1 and OBS2 (MGT 5).

Figure 5: Typical tripod deployed during the MGT campaign.

Figure 6: MCR model grid for flow and waves. Dashed lines indicate the boundaries of the 3 subdomains for sea, estuary and river. Dashed grey ocean domain shows the extend of the wave grid. Top right insert: details computational grid at the MCR.

Figure 7: Time series of observations (solid line) and model results (dashed) at station MGT 4. From top to bottom: (a) water levels, (b) significant wave height, (c) mean absolute wave period, (d) salinity, (e) depth-averaged velocity, and (f) velocity at ADV location (1.2 m above the bed).

Figure 8 (top panels): Modeled depth-averaged flow at (a) max flood tide (22 August 09:00), (b) max ebb tide (22 August 13:00). Month-averaged residual flow velocities in the top (c) and bottom layers (d). (e). Measured and modeled maximum ebb and flood flow at stations MGT 1-5 (left to right).

Figure 9: Comparison of the observed (solid line) and modeled (dashed) tidal velocity ellipses at MGT1-5 in the (a) upper, (b) middle and (c) bottom layers.

Figure 10: (a) Comparison of the observed (dots) and modeled residual flow. (b) Comparison of the mean peak ebb and flood currents. Both plots are averaged over MGT1-5 and relative to the total water depth. The dashed and dash-dot line illustrate the importance of salinity and wind and

waves respectively. An estimate of the salinity contribution is obtained by running a simulation with tides and a saline river discharge as forcing. Wind and wave contributions are estimated by running with tides and river discharge only.

Figure 11: Scatter plot results of wave model at MGT4 for the entire MGT experiment. Shown are results for top-layer (left), depth-averaged (center) and wave-weighted (right). See equations 16, 17 and 18 for definition of Rel. bias, SI and BCSI.

Figure 12: Influence of current profile averaging in the MCR. Spatial results of Hm0 (left) and current fields (right) on 22 Aug 2005 14:00. Shown are results for (a) top-layer, (b) depth-averaged and (c) wave-weighted methods.

Table 1: Summary of observation stations and data used in this study.

Station	Lat. Long.	X <sup>(1)</sup> Y	Data Source	Wind	Waves	Water levels	Current	Salinity
	[°N °W]	[km]						
NDBC 46029 <sup>(2)</sup>	46.1440 124.5100	190.330 97.979	NOAA	X	X			
MGT 1	46.2708 124.0577	225.869 110.382	USGS			X	X	
MGT 2	46.2629 124.0594	225.698 109.510	USGS			X	X	X
MGT 3	46.2573 124.0547	226.032 108.872	USGS			X	X	
MGT 4	46.2510 124.0600	225.276 108.206	USGS		X	X	X	
MGT 5	46.2398 124.0673	224.974 106.974	USGS		X	X	X	X
Astoria <sup>(3)</sup>	46.2083 123.7667	247992.78 102475.01	NOAA			X		
Skamokawa <sup>(3)</sup>	46.2667 123.452	272524.09 107996.22	NOAA					
Beaver <sup>(3)</sup>	46.1806 123.182	292957.42 97693.91	USGS			X	X	
red26	46.207 123.951	233676.88 102917.38	SATURN <sup>(4)</sup>					X
dsdma	46.2257 123.955	233460.93 105040.63	SATURN					X
grays	46.2735 123.767	248167.29 109642.47	SATURN					X
coaof	46.205 123.774	247314.67 102113.36	SATURN					X
cbnc3	46.2095 123.716	251963.87 102478.27	SATURN					X

(1) Coordinate system: Washington State Plane South.

(2) [http://www.ndbc.noaa.gov/station\\_page.php?station=46029](http://www.ndbc.noaa.gov/station_page.php?station=46029)

(3) <http://tidesandcurrents.noaa.gov>

(4) [http://ida.water.usgs.gov/ida/available\\_records.cfm?sn=14246900](http://ida.water.usgs.gov/ida/available_records.cfm?sn=14246900)

(5) The SATURN observation network is operated by the Center for Coastal Margin Observation & Prediction (CMOP), under the direction of Dr. Antonio Baptista and with support from the National Science Foundation (OCE-0424602), the National Oceanic and Atmospheric Administration (NOAA Fisheries and NANOOS), U. S. Army Corps of Engineers, Bonneville Power Administration, Office of Naval Research, and the M. J. Murdock Charitable Trust. ([http://www.stccmop.org/datamart/observation\\_network](http://www.stccmop.org/datamart/observation_network))

Table 2: Calibrated tidal constituents at the center of the open-sea model boundary (facing the MCR).

Constituent	Amp (m)	Phase (deg)
A0	0.000	
M2	0.920	224
K1	0.425	233
S2	0.266	247
O1	0.266	218
N2	0.190	199
P1	0.129	230
K2	0.070	239
NO1	0.056	194
Q1	0.055	210

Table 3: Differences in water level amplitude and phases for the 6 main tidal constituents.

Station		Constituent											
		M2		K1		S2		O1		N2		P1	
		(m)	(°)										
MGT4	obs	0.91	230	0.42	220	0.30	270	0.27	220	0.18	207	0.13	233
	mod	<i>0.91</i>	<i>230</i>	<i>0.42</i>	<i>220</i>	<i>0.30</i>	<i>270</i>	<i>0.27</i>	<i>220</i>	<i>0.18</i>	<i>207</i>	<i>0.13</i>	<i>233</i>
Astoria	obs	0.93	264	0.39	256	0.27	314	0.24	243	0.18	242	0.12	252
	mod	<i>0.88</i>	<i>264</i>	<i>0.38</i>	<i>258</i>	<i>0.26</i>	<i>312</i>	<i>0.26</i>	<i>242</i>	<i>0.16</i>	<i>244</i>	<i>0.11</i>	<i>255</i>
Skamokawa	obs	0.84	292	0.32	273	0.25	343	0.19	262	0.15	271	0.10	270
	mod	<i>0.79</i>	<i>288</i>	<i>0.31</i>	<i>275</i>	<i>0.22</i>	<i>340</i>	<i>0.22</i>	<i>260</i>	<i>0.14</i>	<i>271</i>	<i>0.09</i>	<i>272</i>
Beaver	obs	0.64	317	0.24	294	0.19	10	0.15	290	0.12	298	0.08	291
	mod	<i>0.64</i>	<i>303</i>	<i>0.25</i>	<i>290</i>	<i>0.17</i>	<i>358</i>	<i>0.19</i>	<i>271</i>	<i>0.11</i>	<i>290</i>	<i>0.08</i>	<i>288</i>

Table 4: Model Skill and RMS errors for salinity

Station	Model Skill	Rmse (ppt)
MGT3	0.90	3.0
MGT5	0.87	1.6
red26	0.90	4.7
dsdma	0.96	2.9
grays	0.83	1.7
coaof	0.86	2.1
cbnc3	0.69	2.0

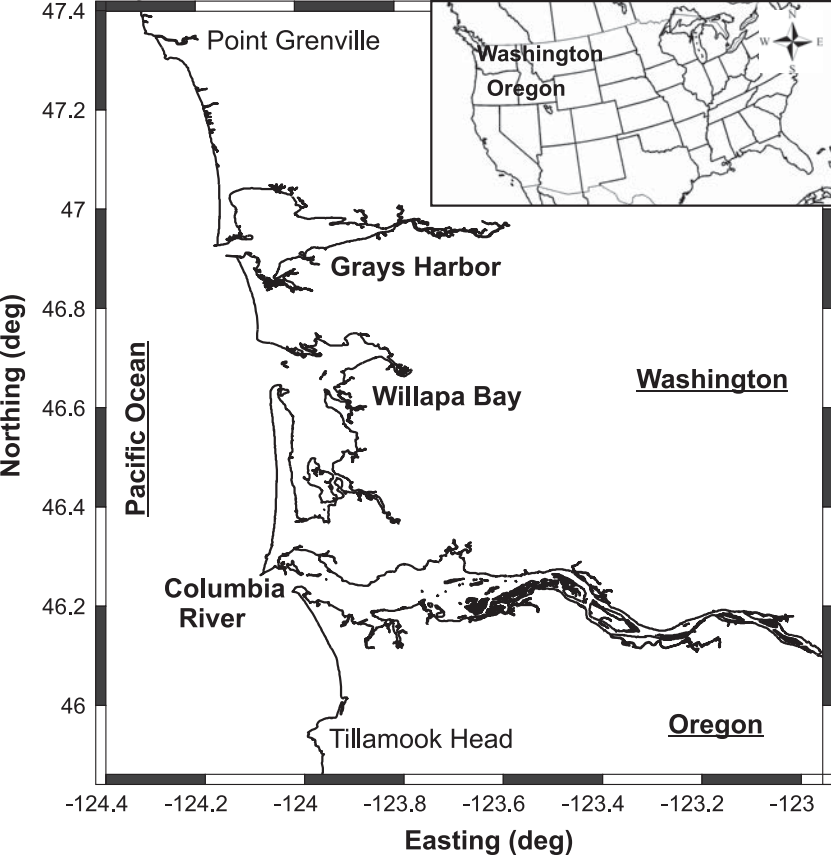
Table 5: Comparison of RMS errors, model skill (Willmott 1984) and residual flow for MGT 1 to 5

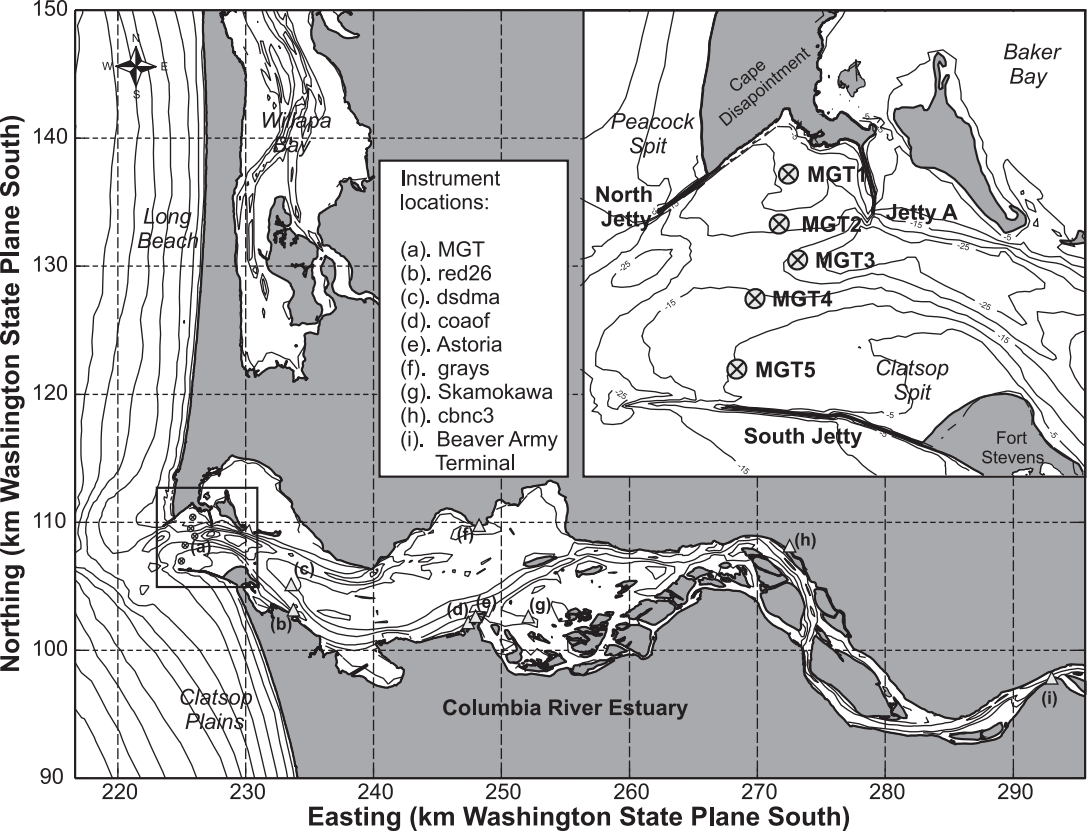
Station	RMS [m/s]			Model Skill [-]			Residual flow [m/s] (bottom bin)	
	MSL	middle	bed	MSL	middle	bed	obs	model
MGT1	0.39	0.22	0.12	0.74	0.95	0.92	0.15	0.15
MGT2	0.47	0.21	0.16	0.89	0.99	0.97	0.02	0.03
MGT3	0.39	0.22	0.19	0.94	0.99	0.98	0.09	0.15
MGT4	0.44	0.24	0.16	0.95	0.99	0.99	0.12	0.14
MGT5	0.44	0.31	0.20	0.91	0.96	0.94	0.02	0.15

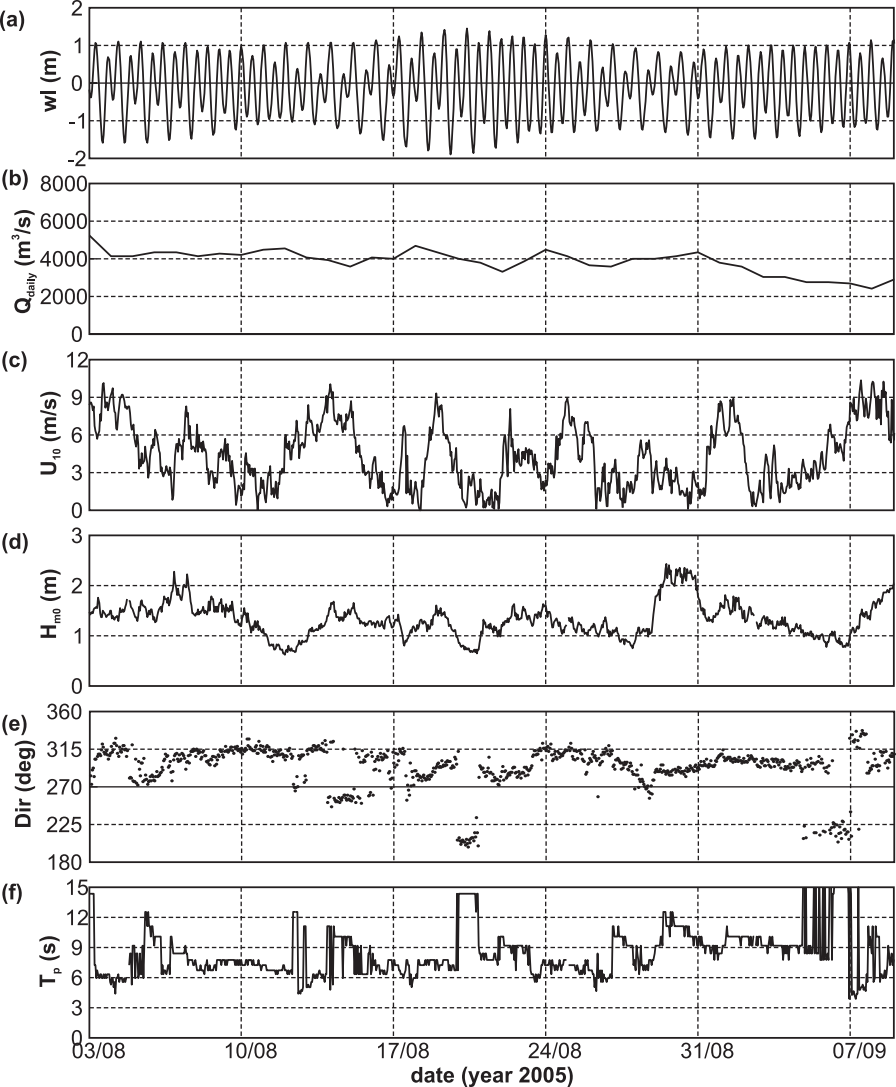
1 Table 6: Summary of the statistical results for waves at MGT4.

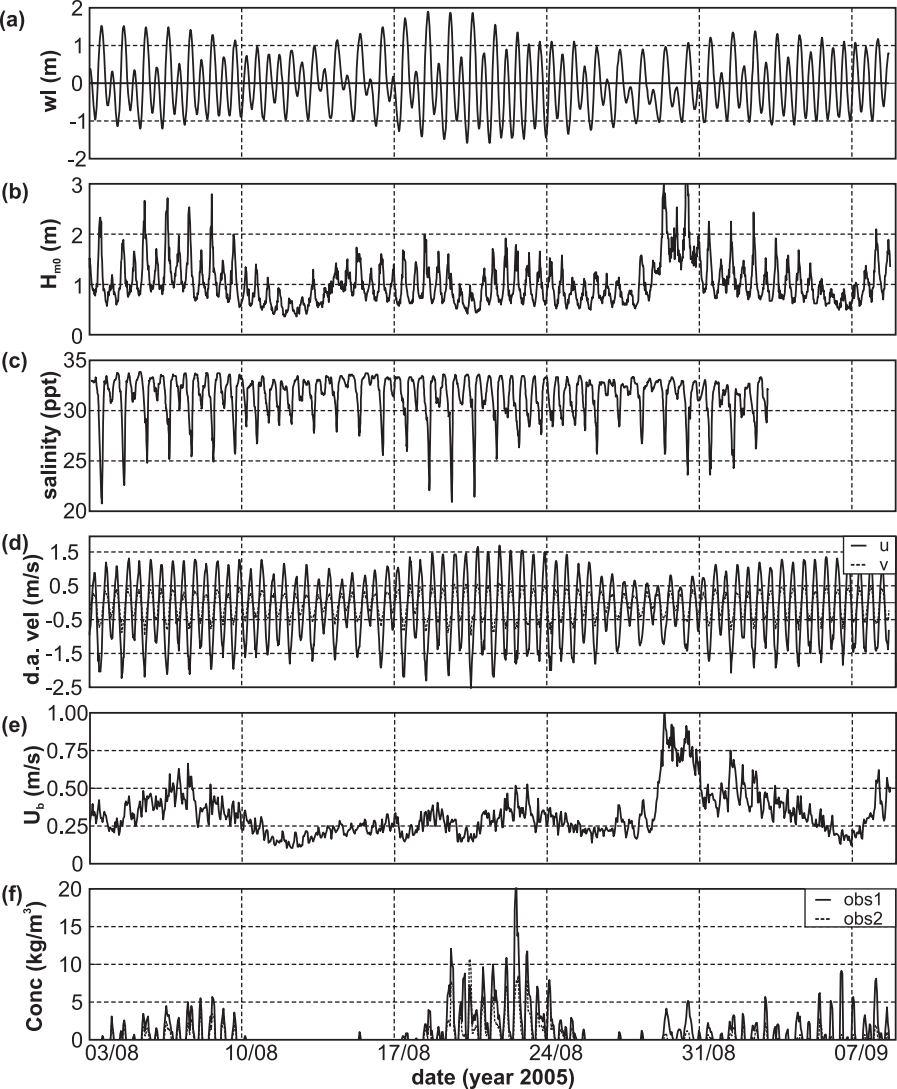
RunID	Model Settings		Statistics			
	$\overline{U}^{(1)}$	$CF_{jon}$ ( $m^2/s^3$ )	Rel. Bias $H_{m0}$	SI $H_{m0}$	Rel Bias $T_{m01}$	SI $T_{m01}$
1	13	0.067	-0.059	0.221	0.011	0.092
2	14	0.067	-0.124	0.234	-0.035	0.125
3	15	0.067	-0.067	0.205	-0.006	0.098
4 (default)	15	0.038	-0.036	0.195	0.006	0.099

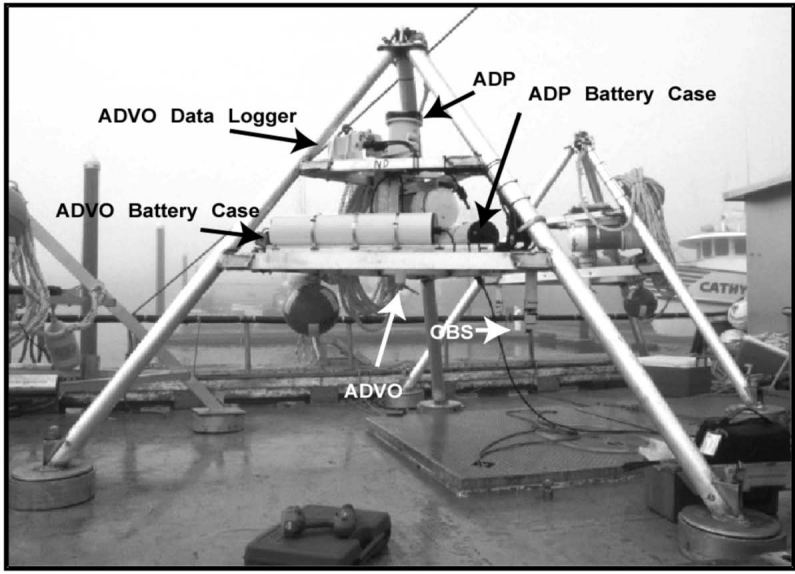
2 (1) formulation used to calculate the flow velocities used in SWAN











ADVOC Data Logger

ADP

ADP Battery Case

ADVOC Battery Case

OBS

ADVOC

CATHY

